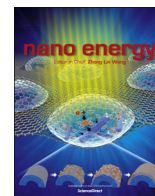




ELSEVIER

Contents lists available at ScienceDirect

Nano Energy

journal homepage: www.elsevier.com/locate/nanoen

Tuning Cu dopant of Zn_{0.5}Cd_{0.5}S nanocrystals enables high-performance photocatalytic H₂ evolution from water splitting under visible-light irradiation

Zongwei Mei^{a,1}, Bingkai Zhang^{a,1}, Jiabin Zheng^a, Sheng Yuan^a, Zengqing Zhuo^{a,b},
 Xianguang Meng^c, Zonghai Chen^d, Khalil Amine^{a,d}, Wanli Yang^{a,b}, Lin.-Wang Wang^{a,e},
 Wei Wang^f, Shufeng Wang^f, Qihuang Gong^f, Jun Li^g, Fu.-Sheng Liu^h, Feng Pan^{a,*}

^a School of Advanced Materials, Peking University Shenzhen Graduate School, 2199 Lishui Road, Shenzhen 518055, China

^b Advanced Light Source, Lawrence Berkeley National Laboratory, 1 Cyclotron Road, Berkeley, CA 94720, United States

^c Environmental Remediation Materials Unit and International Center for Materials Nanoarchitectonics (WPI-MANA), 1-1 Namiki, Tsukuba, Ibaraki 305-0044, Japan

^d Electrochemical Technology Program, Chemical Sciences and Engineering Division, Argonne National Laboratory, Argonne, IL 60439, United States

^e Materials Science Division, Lawrence Berkeley National Laboratory, 1 Cyclotron Road, Berkeley, CA 94720, United States

^f State Key Laboratory for Artificial Microstructure and Mesoscopic Physics, Department of Physics, Peking University, Beijing 100871, China

^g Research Institute of Superconductor Electronics (RISE), Nanjing University, No.163 Xianlin Ave, Nanjing 210046, China

^h College of Materials Science and Engineering, Shenzhen University, 3688 Nanhai Road, Shenzhen 518060, China

ARTICLE INFO

Article history:

Received 20 February 2016

Received in revised form

7 May 2016

Accepted 30 May 2016

Available online 1 June 2016

Keywords:

Cu dopant

Zn_{0.5}Cd_{0.5}S

Mechanism

Photocatalytic H₂ evolution

Water splitting

Visible light

ABSTRACT

Cu-doping into Zn_{1-x}Cd_xS can greatly enhance the photocatalytic H₂ evolution from water splitting under visible-light irradiation. However, it is still controversial for how the Cu-dopant improves this performance. Here, we report that appropriate Cu-doped Zn_{0.5}Cd_{0.5}S nanocrystals reach 21.4 mmol/h/g of H₂ evolution rate without cocatalyst in the visible-light region, which is also 2.8 times as high as that of the undoped counterpart, and the corresponding apparent quantum efficiency is 18.8% at 428 nm. It is firstly confirmed that the Cu²⁺ changes into Cu⁺ after being doped by soft X-ray absorption spectroscopy (sXAS). We theoretically propose that the transformation of 2Cu²⁺ to 2Cu⁺ results in one adjacent S²⁻ vacancy (V_S) in host during the doping process, while the Cu⁺-dopant and V_S attract the photoexcited holes and electrons, respectively. Accordingly, the photocatalytic activity is improved due to the enhanced separation of photoexcited carriers accompanied with the enhanced light absorption resulting from the Cu⁺-dopant and 2Cu⁺/V_S complex as possible active site for photocatalytic H₂ evolution.

© 2016 Elsevier Ltd. All rights reserved.

1. Introduction

The transformation of solar energy into clean H₂ by photocatalytic water splitting is attracting growing research interest due to the worldwide desire to decrease the use of fossil fuels and reduce accompanying environmental problems. For photocatalysis, it is still crucial to understand how to improve the light-absorption and solar-energy-conversion efficiency [1,2], although significant achievements have already been made to date.

In semiconductor photocatalysts, three main steps dominate the performance of photocatalytic H₂ evolution reduction (HER) in water splitting. The first is the excitation by photons with larger energy than the band gap, in which the performance is directly

determined by the amount of light absorbed and the band gap of the photocatalysts; The second step is the transportation of the unrecombined photoexcited carriers to the surface, in which appropriate trapping states [3], shorter transfer distance and quantum confinement effects of nanocrystals are beneficial to avoid the rapid recombination [4–6]. The final step is the effective reduction of H⁺ to H₂, which can be improved by optimizing kinetic process of photoexcited electrons at the catalyst interfaces, including loading cocatalysts [7] and increasing surface area-to volume ratio with more active sites for surface redox reactions [5,8–10] and so on.

Recently, transition metal sulfides, such as ZnS-based materials, have been reported to be effective H₂ evolution photocatalysts with high performance without cocatalysts [11]. Although ZnS is only responsive to UV light owing to its wide band gap, ZnS-based solid solutions, such as (AgIn)_xZn_{2(1-x)}S [12], ZnS-CuInS₂-AgInS₂ [13,14], ZnS-In₂S₃-CuS [15], and ZnS-In₂S₃-Ag₂S [16], are good

* Corresponding author.

¹ These authors contributed equally to this work.

candidates for photocatalytic water splitting under visible-light irradiation. Additionally, the $\text{Zn}_{1-x}\text{Cd}_x\text{S}$ solid solution, combining the highly photocatalytic activity of ZnS with the visible-light absorption of CdS, shows good photocatalytic H_2 evolution performance even without any cocatalyst [17–19]. In order to further improve the separation and migration of the photoinduced carriers, besides the coupling composites [20–22], adjusting the dopant is another effective way, for example, Ni^{2+} doped $\text{Zn}_x\text{Cd}_{1-x}\text{S}$ photocatalyst can significantly enhance the photocatalytic activity [23,24]. Furthermore, surface dopants of Ba [25], Sr [26], and La [27] show better performance than undoped materials. The Cu^{2+} doping into $\text{Zn}_{1-x}\text{Cd}_x\text{S}$ has also been considered intensively as the Cu dopant has been shown to greatly enhance the photocatalytic activities [28–30]. It was proposed that the bulk dopants or surface dopants could introduce accommodation sites for the separation of photoinduced carriers and accordingly enhance the photocatalytic activities. Importantly it is still controversial that how the copper dopant improves the separation capability of the photo-generated carriers and accordingly enhances the photocatalytic activities, that is to say whether the Cu dopant attracts the photoexcited electrons or holes [15,28–30]. It is thus critical to understand the underlying mechanism for how the Cu doping can improve the photocatalytic water splitting efficiency, and what the possible active site is.

Herein, mesoporous $\text{Zn}_{0.5}\text{Cd}_{0.5}\text{S}$ by nanocrystals aggregation with controlled copper dopant and large surface area was successfully synthesized by a simple solvothermal method. By the characterization of soft X-ray absorption spectroscopy (sXAS), it was found that the starting Cu^{2+} -dopant source turned into Cu^+ in the $\text{Zn}_{0.5}\text{Cd}_{0.5}\text{S}$ host, and Cu^0 clusters were not found in the whole doped $\text{Zn}_{0.5}\text{Cd}_{0.5}\text{S}$, which is known to be efficient photocatalytic HER cocatalyst [31]. The highest 21.4 mmol/h/g of photocatalytic H_2 evolution rate of mesoporous $\text{Zn}_{0.5}\text{Cd}_{0.5}\text{S}$ with appropriate Cu^+ -dopant was achieved for the first time, which was about 2.8 times as high as that of the undoped $\text{Zn}_{0.5}\text{Cd}_{0.5}\text{S}$. Based on the density functional theory (DFT) calculation results, the change of Cu^{2+} into Cu^+ -dopant would result in adjacent S^{2-} vacancies (V_S) in $\text{Zn}_{0.5}\text{Cd}_{0.5}\text{S}$, and the doped Cu^+ and the V_S could act as the photoexcited hole and electron trapping positions,

respectively. Accordingly, the $2\text{Cu}^+/V_S$ complex on the surface of mesoporous $\text{Zn}_{0.5}\text{Cd}_{0.5}\text{S}$ would be carrier sinks and possible active sites of HER, which accompanying with enhanced light absorption improved the photocatalytic activities for H_2 evolution, although those S^{2-} vacancies in the core of mesoporous catalyst could be recombination centers that decreased photocatalytic activities (Scheme 1).

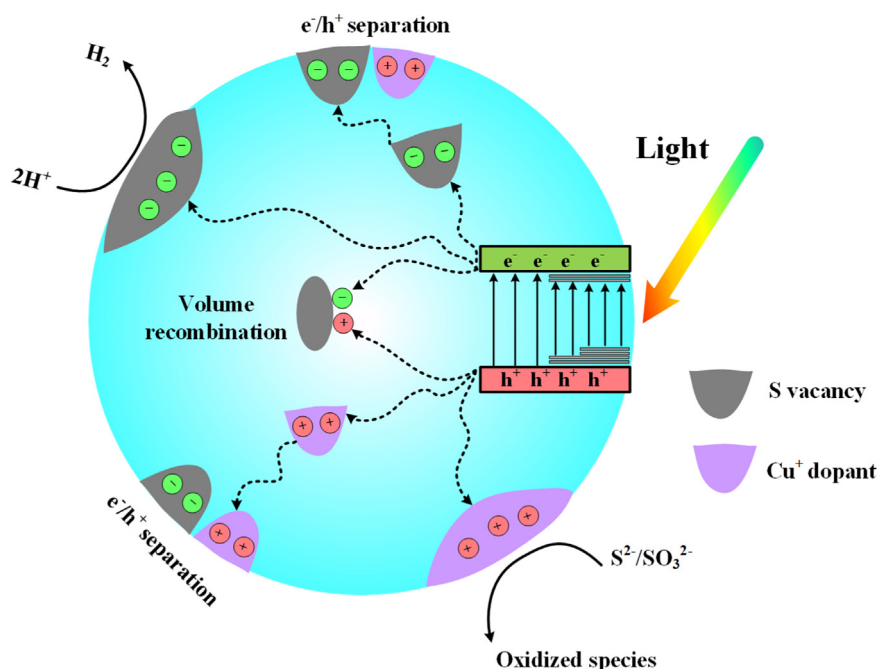
2. Experimental section

2.1. Materials

The starting materials include $\text{Cu}(\text{CH}_3\text{COO})_2 \cdot \text{H}_2\text{O}$ (AR, Sino-pharm Chemical Reagent CO., Ltd., China), $\text{CdCl}_2 \cdot 2.5\text{H}_2\text{O}$ (AR, Tianjin BASF Chemical CO., Ltd., China), $\text{Zn}(\text{CH}_3\text{COO})_2 \cdot 2\text{H}_2\text{O}$ (AR, Aladdin Industrial Corporation, China), diethanolamine (AR, Aladdin Industrial Corporation, China), ethylene glycol (AR, Shanghai Titan Scientific CO., Ltd., China), ethanol (AR, Shanghai Titan Scientific CO., Ltd., China), and $\text{Na}_2\text{S} \cdot 9\text{H}_2\text{O}$ (AR, Aladdin Industrial Corporation, China).

2.2. Preparation of Cu-ZCS(x%)

Photocatalysts with copper dopant in the mesoporous $\text{Zn}_{0.5-x}\text{Cd}_{0.5}\text{Cu}_x\text{S}$ ($x=1-5\%$) aggregated by nanocrystals with sizes of 4–6 nm [thereafter named Cu-ZCS(x%)] were synthesized by a solvothermal method using diethanolamine as the complexing agent. In a typical synthesis procedure, $6(0.5-x)$ mmol of $\text{Zn}(\text{CH}_3\text{COO})_2 \cdot 2\text{H}_2\text{O}$, 3 mmol of $\text{CdCl}_2 \cdot 2.5\text{H}_2\text{O}$, and $6x$ mmol of $\text{Cu}(\text{CH}_3\text{COO})_2 \cdot \text{H}_2\text{O}$, in which x varies from 0.01 to 0.05, were dissolved in 50 ml of ethylene glycol by magnetic stirring. Then, 1 ml of diethanolamine was added into the above solution. After 20 min, 50 ml of ethylene glycol with 6.5 mmol of dissolved $\text{Na}_2\text{S} \cdot 9\text{H}_2\text{O}$ was dripped into the above solution in 30 min for the deposition of the metal ions. After being stirred for 15 min, the solution with Cu-doped $\text{Zn}_{0.5}\text{Cd}_{0.5}\text{S}$ was transferred into a Teflon liner with 200 ml capacity, and 50 ml ethanol was added. Then, the liner was sealed by a stainless steel autoclave, which was



Scheme 1. Scheme of the enhanced photocatalytic H_2 evolution performance by the surface Cu^+ -dopant and the volume recombination centers of photoexcited carriers induced by the core Cu^+ -dopant in mesoporous $\text{Zn}_{0.5}\text{Cd}_{0.5}\text{S}$.

heated at 140 °C for 12 h in an oven. Next, the whole system was cooled to room temperature, and the products were cleaned three times using distilled water and ethanol. Finally, the cleaned products were dried in a vacuum oven at 60 °C for 12 h.

2.3. Preparation of ZnS, CdS, CuS, and Zn_{0.5}Cd_{0.5}S (ZCS)

The procedures are the same as that of the Cu-ZCS(x%), except for the kinds and amount of the added metal salts.

3. Characterization

The crystal structure of the photocatalysts was characterized by XRD using a D8 Advance (Germany) with Cu K α radiation ($\lambda=0.15406$ nm). The typical transmission electron microscopy (TEM) and high-resolution TEM (HRTEM) images were characterized by TEI Tecnai G2 F30 at 300 kV. The Brunauer-Emmett-Teller (BET) surface area and pore size distribution were obtained by nitrogen adsorption at 77 K using an Accelerated Surface Area and Porosimetry System (ASAP 2020 HD88). Room temperature UV–vis absorption was recorded with a UV-2450 spectrophotometer. The atomic ratio characterization was obtained with inductively coupled plasma-atomic emission spectroscopy (JY2000-2). The photoluminescence spectra were recorded by a UV/V/NIR Fluorescence Spectrometer FLS 9802. The Cu *L*-edge X-ray absorption spectroscopy (XAS) was performed at beamline 8.0.1 of the Advanced Light Source (ALS) at Lawrence Berkeley National Laboratory (LBNL). The undulator and spherical grating monochromator supplied a linearly polarized photon beam with resolving power up to 6000. The experimental energy resolution was better than 0.15 eV. All the XAS experiments were performed at room temperature. All the spectra were collected in the surface-sensitive total electron yield (TEY) and bulk-sensitive total fluorescence yield (TFY) modes. The probing depth was around 5–10 nm for the TEY mode and 150 nm for the TFY mode. All the spectra were normalized to the photon flux measured by the photocurrent of an upstream gold mesh. Extended X-ray absorption fine structure spectroscopy (EXAFS) experiments were performed at the K-edge of Zn (around 9668.55 eV) to monitor the change of the local environment of Zn.

4. Photocatalytic test

The photocatalytic activities of the materials were carried out in a quartz-cell reactor with a side window, which was connected to a closed gas-circulation system. In each test, about 0.1 g of the photocatalyst powder was added into the reactor, including 300 ml of Na₂S (0.35 M)/Na₂SO₃ (0.25 M) aqueous solution. Visible light ($\lambda \geq 420$ nm) was generated by a 300 W Xe lamp combined with a UV-cut-off filter (UVCUT 420, AU-LIGHT Co. Ltd., China). The evolved H₂ was analyzed by an on-line gas chromatograph [GC7900(T), TECHCOMP, China] equipped with a thermal conductivity detector. All evolved H₂ from the samples was tested every hour during three hours of a cycle. The AQE was measured by applying LED lights (Shenzhen Lamplic Science Co., LTD, China). The number of incident photons was measured with a radiant power energy meter (Ushio Spectroradiometer, USR-40). The AQE was calculated from the following equation:

$$\begin{aligned} \text{AQE}(\%) &= \frac{\text{The number of reacted electrons}}{\text{The number of incident photons}} \times 100\% \\ &= \frac{2 \times \text{The number of evolved H}_2 \text{ molecules}}{\text{The number of incident photons}} \times 100\% \end{aligned} \quad (1)$$

5. Computational details

The geometric and electronic structures were determined by the spin-polarized density functional theory (DFT) [32,33] within the generalized gradient approximation (GGA) and Perdew-Burke-Ernzerhof (PBE) functions [34], implemented via the Vienna Ab Initio Simulation (VASP) package [35]. The details of DFT method are shown as following. A force and energy convergence of 0.01 eV/Å and 10⁻⁵ eV, respectively, were achieved using an energy cutoff of 400 eV for the plane-wave expansion of the electronic wave function. The DFT+U method was used to treat the strong on-site Coulomb interaction of Zn, Cd, and Cu *d* state. The values of U=7.0, 7.0, and 6.0 were set for Zn 3*d* states, Cd 4*d* states, and Cu 3*d* states, respectively [36].

To find the most stable arrangement of the substitutional atoms (Cd and Zn) in the ZCS solid solution (Zn, 50%), we randomly build six different configurations using a 16-atom (1 × 2 × 1) supercell, as shown in Fig. S1 (Supporting Information, SI). We found that total energies of six different configurations of the ZCS in Fig. S1 are very close (−47.49, −47.45, −47.63, −47.45, −47.45, and −47.49 eV). Moreover, we found that the electronic structures of the ZCS solid solution have a configuration-independent feature (Fig. S2). To test the reliability of the size of the supercell, we calculated the CZSZCS solid solution (Zn, 50%) by a (2 × 2 × 2) supercell. We also found the energies of different configurations are very close. Thus, the arrangement of the substitutional atoms (Cd and Zn) in the ZCS solid solution can be considered random.

To save computing resources and time, a (2 × 2 × 2) supercell of ZCS with two Cu atoms was built (the concentration of Cu in the model is 6.25%) by combining four different (1 × 2 × 1) supercell models. Then, we calculated the structural and electronic properties of a (4 × 3 × 2) supercell of ZCS with two Cu atoms. The impurity concentration is about 2.08%, which is comparable to that in the experiment. We found that relative to the results calculated from the (2 × 2 × 2) supercell, the lattice parameters (5.660 Å) and the electronic structures of the solid solution are retained except intensity (Figs. S3 and S4). The electronic states of Cu atoms stay at the same position in the two models. Thus, the (2 × 2 × 2) supercell is adequate for the study of the structural and electronic properties herein.

To further test the reliability of the size of the supercell, we first compared the calculated lattice parameters and simulated XRD patterns with those of experiments. The lattice constant for bulk Cu-ZCS is calculated to be 5.656 Å, which is close to the experimental value of 5.634 Å [Cu-ZCS(5%)]. The comparison of simulated and experimental XRD patterns is shown in Fig. S5. The location of major spectrum peaks in simulated and experimental results is in good agreement. In addition, the valence state of Cu was justified by comparing Bader charge of Cu in different phases of CuS and Cu₂S. We found that there was small difference of Bader charge between Cu₂S and CuS, which may come from the so-called charge-self regulation mechanism [37]. The Bader charge of Cu in Cu-ZCS is 10.64e and locates within the range of isolated Cu₂S phases, suggesting Cu¹⁺ in the Cu-ZCS model.

In the cubic ZnS, (110) and (111) were the two most stable terminal surfaces. Thus, a 3 × 2 slab with 4 layers and 72 atoms was employed to model the ZCS(110) surface. A vacuum region of 20 Å was introduced to minimize interactions between periodic slabs. A 3 × 3 slab with 3 layers and 144 atoms was employed to model the ZCS(111) surface. The positions of all atoms were allowed to relax. The (111) surface is a polar one with a S-terminal and Cd/Zn-terminal, respectively. The dipole terminals may induce large dipole moments at the surface. Therefore, a OH_{1.5} (H with 1.5 positive charge) was used to passivate the Cd/Zn-terminal, and H_{0.5} (H with 0.5 positive charge) was used to passivate the S-terminal. The similarity surface passivation was done by previous studies [38]. The

$3 \times 3 \times 3$ Monkhorst-Pack grid was used for the ZCS supercells. A $2 \times 2 \times 1$ grid was used for the (110) and (111) surfaces. The detailed configurations are shown in Figs. S6 and S7.

The formation energy of Cu substitution and S vacancy with q charge state was calculated as follows:

$$E_{\text{form}} = E_{\text{doped}} - E_{\text{pure}} + (E_{\text{Zn}} + \Delta\mu_{\text{Zn}}) - (E_{\text{Cu}} + \Delta\mu_{\text{Cu}}) + q(\epsilon_{\text{VBM}} + E_{\text{F}} + \Delta\nu) \quad (2)$$

$$E_{\text{form}} = E_{\text{S-vacancy}} - E_{\text{pure}} + (E_{\text{S}} + \Delta\mu_{\text{S}}) + q(\epsilon_{\text{VBM}} + E_{\text{F}} + \Delta\nu) \quad (3)$$

respectively. E_{doped} and E_{pure} are the total energies of the doped and undoped systems, respectively; and $\Delta\mu_{\text{Zn}}$ and $\Delta\mu_{\text{Cu}}$ are the chemical potentials of Zn atom and Cu, referenced to the total energy of hexagonal-closed pack Zn (E_{Zn}) and face-centered cubic Cu (E_{Cu}), respectively. $\Delta\mu_{\text{S}}$ is referenced to the one-sixth of the total energy of the S_6 molecule in the gas phase (E_{S}). E_{F} is the Fermi energy level referenced to the VBM eigen energy of the bulk ZCS system, and ϵ_{VBM} is the VBM eigen energy of the bulk system when the averaged Hartree potential is set to zero. The term is added for correction of the electrostatic potential caused by the limited size of the supercell, obtained by taking the shifting of the 1s core-level energy of a Zn atom (located far away from the defect site) between the neutral impurity and charged cases.

Before we calculated the formation energy, we first determine the chemical potential values of Zn, Cu, and S by plotting stability diagram of Cu-ZCS. Here, we selected the calculated $\text{Cu}_2\text{Zn}_{14}\text{Cd}_{16}\text{S}_{32}$ (CZCS)(Cu-ZCS) model as the stability phase. In equilibrium growth condition of Cu-ZCS, to avoid the occurrences of these secondary phases, the following conditions have to be satisfied:

$$\Delta\mu_{\text{Zn}} + \Delta\mu_{\text{S}} \leq \Delta H_{\text{f}}[\text{ZnS}] = -2.0 \text{ eV} \quad (4)$$

$$\Delta\mu_{\text{Cd}} + \Delta\mu_{\text{S}} \leq \Delta H_{\text{f}}[\text{CdS}] = -1.64 \text{ eV} \quad (5)$$

$$\Delta\mu_{\text{Cu}} + \Delta\mu_{\text{S}} \leq \Delta H_{\text{f}}[\text{CuS}] = -0.50 \text{ eV} \quad (6)$$

$$2\Delta\mu_{\text{Cu}} + \Delta\mu_{\text{S}} \leq \Delta H_{\text{f}}[\text{Cu}_2\text{S}] = -0.81 \text{ eV} \quad (7)$$

To form a stable stoichiometric $\text{Cu}_2\text{Zn}_{14}\text{Cd}_{16}\text{S}_{32}$, the necessary thermodynamics condition is

$$\Delta\mu_{\text{Cu}} + 7\Delta\mu_{\text{Zn}} + 8\Delta\mu_{\text{Cd}} + 16\Delta\mu_{\text{S}} \leq \Delta H_{\text{f}}[\text{Cu-ZCS}] = -26.41 \text{ eV} \quad (8)$$

6. Results and discussion

6.1. Characterization of the as-synthesized materials

Fig. S8 shows the typical X-ray diffraction (XRD) patterns of the as-synthesized ZnS, CdS, and $\text{Zn}_{0.5}\text{Cd}_{0.5}\text{S}$ (ZCS). The XRD results indicate that $\text{Zn}_{0.5}\text{Cd}_{0.5}\text{S}$ is a solid solution between the cubic ZnS (JCPDS: PDF-05-0566) and the cubic CdS (JCPDS: PDF-10-0454). Fig. 1(a) exhibits the typical XRD patterns of $\text{Zn}_{0.5}\text{Cd}_{0.5}\text{S}$ and Cu-ZCS(1–5%). The peaks of Cu-ZCS(1–5%) do not exhibit obvious shifts in comparison with those of the corresponding undoped material. The real molar ratios of Zn, Cd, and Cu metal elements in the samples were determined by inductively coupled plasma atomic emission spectroscopy (ICP-AES). The ratios are close to the proportion of the added $\text{Cu}^{2+}/(\text{Zn}^{2+} + \text{Cd}^{2+} + \text{Cu}^{2+})$ as shown in Table 1. The red shift of the UV–vis absorption with increasing Cu dopant indicates that copper was successfully doped into $\text{Zn}_{0.5}\text{Cd}_{0.5}\text{S}$ (Fig. 1(b)). The typical TEM and HRTEM images of $\text{Zn}_{0.5}\text{Cd}_{0.5}\text{S}$ and Cu-ZCS(2%) indicate that the synthesized samples are aggregated by nanoparticles about 4–6 nm in diameter (Fig. 2(a)–(d)), and the interplanar spacings of all the samples are about 3.25 Å, which agrees well with the calculated value of the (111) plane according to the Bragg equation [Eq. (1) in SI]. The BET characterization of $\text{Zn}_{0.5}\text{Cd}_{0.5}\text{S}$ and Cu-ZCS(2%) shows that all the as-synthesized samples are mesoporous structures with about 10 nm of pore size (Fig. 2(e)) and similar high surface area (Table 1). The similar results of TEM, HRTEM, and BET characterizations are also observed in Cu-ZCS(1%, and 3%–5%) as shown in Figs. S9 and S10, respectively.

Soft X-ray absorption spectroscopy (sXAS) can directly probe the transition metal 3d valence states through dipole selection rules [39–41]. The sXAS has advantages over other techniques on probing the key electronic states in the vicinity of the Fermi level, relevant to valency, spin states, and local structural effects on the crystal field. For example, there is little difference between the two peaks of Cu^+ [42,43] and Cu^{2+} [44,45] characterized by X-ray photoelectron spectroscopy (XPS). However, the sXAS can clearly distinguish Cu^+ and Cu^{2+} [39–41]. Fig. 3(a) and (b) show the Cu L edge XAS TEY (testing signal from the surface of 5–10 nm) and TFY (testing signal from the core of 150 nm in depth) spectra collected on Cu-ZCS(2%, and 5%) and the reference CuS sample synthesized by the same method. The spectra consist of well-separated absorption features in two regions, L3 (922–932 eV) and L2 (942–948 eV), resulting from the 2p core-hole spin-orbital splitting. For Cu L edge soft XAS spectra, a previous study had shown that the overall line shape is sensitive to the different chemical state of the

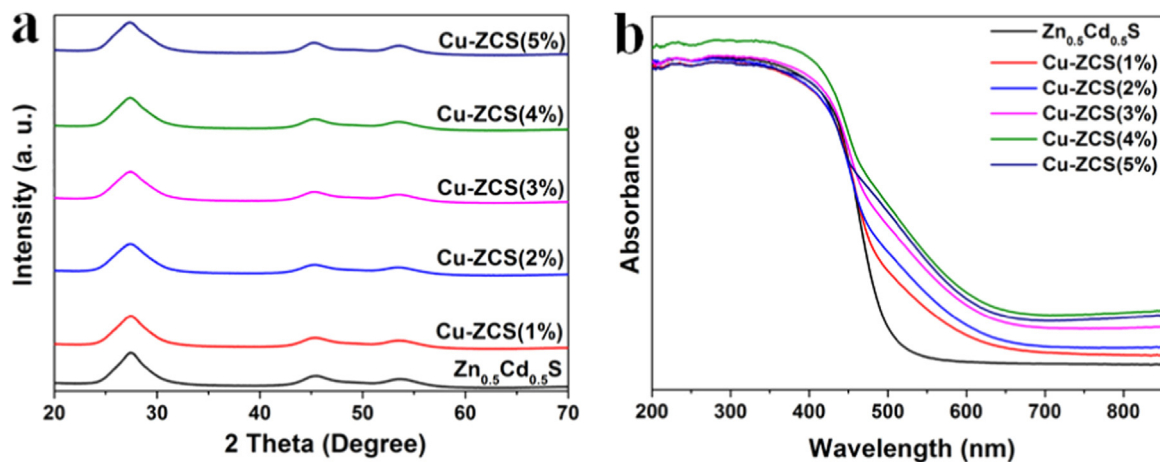


Fig. 1. (a) The XRD patterns and (b) UV–vis absorption spectra of $\text{Zn}_{0.5}\text{Cd}_{0.5}\text{S}$ and Cu-ZCS(1–5%).

Table 1

The molar ratios of metal elements and BET surface of the samples.

Samples	Zn:Cu:Cu (primarily added)	Zn:Cu:Cu (tested)	Surface area (m ² /g)
Zn _{0.5} Cd _{0.5} S	0.5:0.5:0	0.49:0.51:0	162
Cu-ZCS (1%)	0.49:0.5:0.01	0.482:0.507:0.011	202.2
Cu-ZCS (2%)	0.48:0.5:0.02	0.468:0.511:0.022	206.5
Cu-ZCS (3%)	0.47:0.5:0.03	0.46:0.508:0.032	197.7
Cu-ZCS (4%)	0.46:0.5:0.04	0.45:0.508:0.042	167.1
Cu-ZCS (5%)	0.45:0.5:0.05	0.441:0.505:0.053	163.0

copper sulfides [46]. The spectra of copper sulfides with different chemical states show different absorption features, especially on the L3 edge. Just according to the reference [46], there are completely different line-shapes and different peak positions among

Cu²⁺, Cu⁺ and Cu⁰. The energy position of Cu⁺ is about 2.5 eV higher than that of Cu²⁺, and the energy position of Cu⁰ is about 1.5 eV higher than that of Cu²⁺. However, the resolution of our sXAS spectroscopy is much better than that in the reference. That is why there are two sharp features in our CuS XAS (Fig. 3(a) and (b)) compared with the one broad feature in the reference. Fig. 3 (a) and (b) show that the absorption features of Cu-ZCS(2%, and 5%) are totally different from those of the reference CuS, and the difference between the main L3-edge peaks of CuS and Cu-ZCS(2%, and 5%) is about 2.5 eV, which is consistent with the features of Cu⁺ in the previous work [46], indicating that there is only Cu⁺ and no Cu²⁺ in Cu-ZCS(2%, and 5%), and the doped Cu distributes on the surface and in the core parts of the Cu-ZCS(x%) samples. Additionally, it further proves that the copper was successfully doped into the Zn_{0.5}Cd_{0.5}S host due to the absence of a Cu²⁺ signal

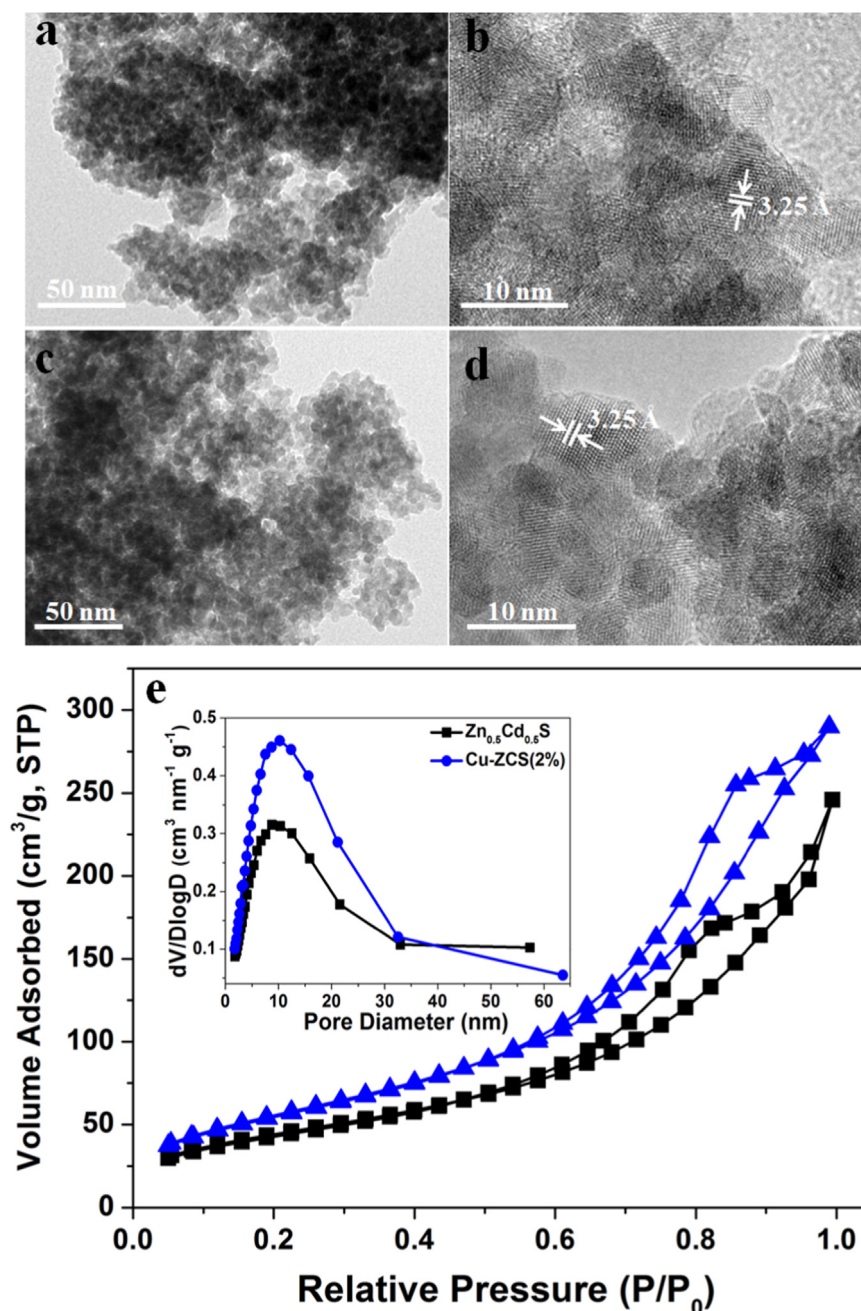


Fig. 2. The typical TEM and HRTEM images of (a, b) Zn_{0.5}Cd_{0.5}S; (c, d) Cu-ZCS(2%); and (e) nitrogen adsorption-desorption isotherms and pore distribution (inset) of Zn_{0.5}Cd_{0.5}S and Cu-ZCS(2%).

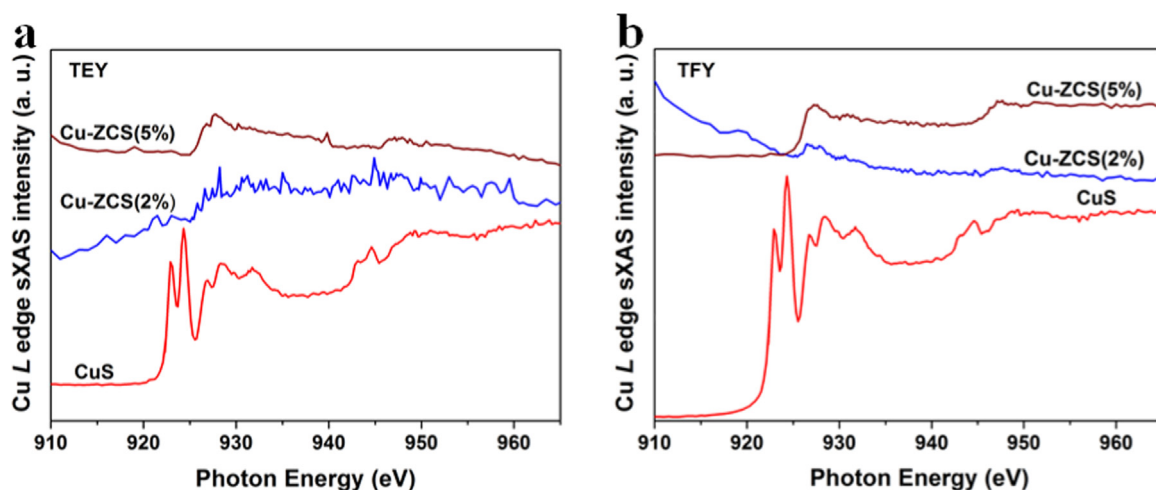


Fig. 3. (a) Cu L edge XAS TEY spectra and (b) Cu L edge XAS TFY spectra collected on samples of Cu-ZCS(2%, and 5%), and the reference CuS.

(hence no separated CuS). There have been several similar reports that the Cu^{2+} source transforms into Cu^+ after being doped into ZnSe or ZnS [47–49]. Furthermore, the previous study has also shown that the energy position of Cu^0 L3-edge main peak is about 1.5 eV higher than that of CuS, and the spectra of Cu^0 L3 edge shows a broad feature [46]. For Cu-ZCS(x%) samples, none such features has been found, indicating that there is no Cu^0 on the surface of the samples in the sensitivity range of the sXAS measurement. Thus, the Cu^{2+} -dopants will not form Cu clusters on the surface of $\text{Zn}_{0.5}\text{Cd}_{0.5}\text{S}$. Compared with TEY mode, TFY mode can get the signal with the sum of 150 nm in depth of small particles. In our work, the Cu^+ signal is detectable with TEY or TFY mode. It can be reasonably concluded that the Cu element was successfully doped into every nanocrystal by our synthesis method, which is different from the surface-rich or inner-rich Cu dopant in previous work [29,30].

6.2. Photocatalytic performance

The photocatalytic H_2 evolution from water splitting was tested under visible-light irradiation ($\lambda \geq 420$ nm) without cocatalyst using Na_2S (0.35 M)/ Na_2SO_3 (0.25 M) as sacrificial reagents in a closed gas-circulation system. The H_2 evolution amount was detected by on-line gas chromatography (details shown in Experimental section). The H_2 evolution rates of these photocatalysts are exhibited in Fig. 4(a), and the time course of H_2 evolution of each

sample is shown in Fig. S11(a). The Cu-ZCS(1–5%) samples show higher photocatalytic H_2 evolution rates than the undoped $\text{Zn}_{0.5}\text{Cd}_{0.5}\text{S}$, and the Cu-ZCS(2%) sample reaches the highest performance to 48 ml/h/0.1 g (equaling about 21.4 mmol/h/g) of H_2 evolution rate, which is around 1.8 times higher than that of $\text{Zn}_{0.5}\text{Cd}_{0.5}\text{S}$ without Cu^+ -doping. The cycle test in Fig. S11(b) shows that there is a little decrease of photocatalytic activity in the third run. The sample of the cycle test was collected and characterized by sXAS. The result in Fig. S12 shows the peak position is in agreement with that of Cu^+ , which means the Cu^+ keep stable before and after photocatalytic H_2 evolution test. Then the decreased photocatalytic activity was probably due to the photocorrosion or the consumption of sacrificial reagents that was common for sulfide photocatalysts [15].

Fig. 4(b) indicates the normalized intensity of the UV–vis absorption of $\text{Zn}_{0.5}\text{Cd}_{0.5}\text{S}$, Cu-ZCS(2%), and the emission spectra of 428 nm, 468 nm, 498 nm, 515 nm, and 590 nm for a light-emitting diode (LED). There is no significant difference for the light absorption of the two samples to the 428 nm LED wavelength. However, $\text{Zn}_{0.5}\text{Cd}_{0.5}\text{S}$ shows a little absorption to 498 nm and 515 nm, and no absorption to 590 nm LED wavelength, which are different from the behavior of Cu-ZCS(2%). The inset in Fig. 4(b) displays the apparent quantum efficiency (AQE) of $\text{Zn}_{0.5}\text{Cd}_{0.5}\text{S}$ and Cu-ZCS(2%) at the above corresponding LED wavelengths. The AQE value of Cu-ZCS(2%) is 18.8% at 428 nm, which is higher than 16.5% of $\text{Zn}_{0.5}\text{Cd}_{0.5}\text{S}$. Additionally, the AQE values are 6.7% and 6.8%

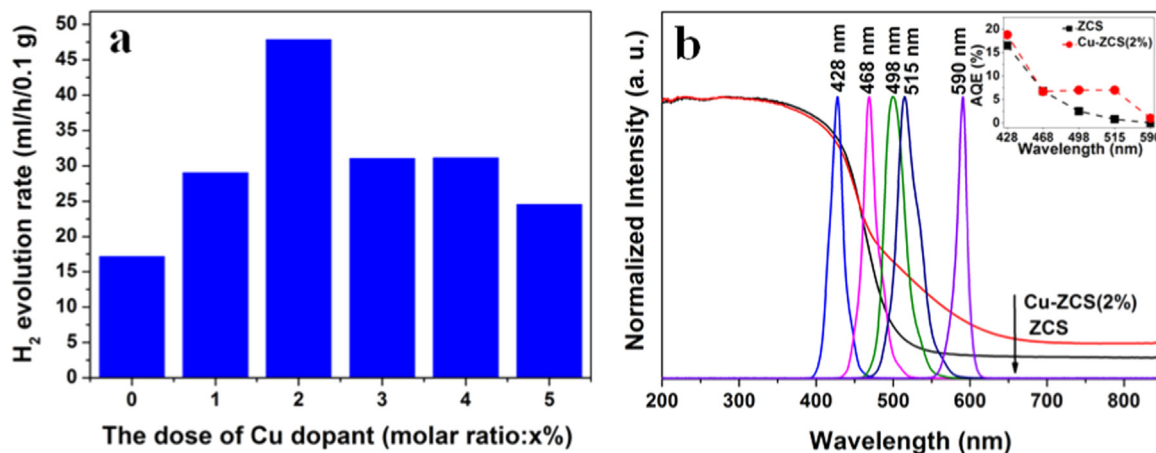


Fig. 4. (a) Photocatalytic H_2 evolution rate of $\text{Zn}_{0.5}\text{Cd}_{0.5}\text{S}$ and Cu-ZCS(1–5%) in 300 ml of Na_2S (0.35 M)/ Na_2SO_3 (0.25 M) aqueous solution under visible-light irradiation ($\lambda \geq 420$ nm) without cocatalyst (added photocatalyst: 0.1 g); (b) normalized intensity of the UV–vis absorption spectra of $\text{Zn}_{0.5}\text{Cd}_{0.5}\text{S}$, Cu-ZCS(2%), and the emission spectra of 428 nm, 468 nm, 498 nm, 515 nm, and 590 nm LED lights. Inset: the AQEs of $\text{Zn}_{0.5}\text{Cd}_{0.5}\text{S}$ and Cu-ZCS(2%) at the above LED wavelengths.

for Cu-ZCS(2%) and $\text{Zn}_{0.5}\text{Cd}_{0.5}\text{S}$ at 468 nm, respectively. However, the AQEs of Cu-ZCS(2%) are around 7%, 7%, and 1% at 498 nm, 515 nm, and 590 nm, respectively, while the AQEs of $\text{Zn}_{0.5}\text{Cd}_{0.5}\text{S}$ are much lower at 498 nm and 515 nm or almost zero at 590 nm due to the poor light absorption at the three above LED wavelengths. We concluded that the enhanced photocatalytic activities are caused by the enhanced AQE under the same and shorter light irradiation and the enhanced light absorption at the longer wavelength caused by the Cu^+ -dopant.

6.3. Theoretical calculation

Although the above experimental results indicate that the Cu^+ -dopant of mesoporous Cu-ZCS(1–5%) greatly enhances the photocatalytic H_2 evolution. To provide insights into the mechanism of Cu doping on the performance of the photocatalysts, we used density functional theory (DFT) calculations to explore possible answers to the following questions: (i) How does the valence state of copper change from +2 to +1? and (ii) What is the role of Cu^+ -dopant in the three main steps of photocatalytic water splitting? To answer these questions, we have calculated the bulk $\text{Zn}_{0.5}\text{Cd}_{0.5}\text{S}$ (ZCS) and (110) and (111) surfaces of ZCS, including clean ones, with defects and Cu^+ -dopants. The detailed DFT method and geometric configurations are shown in Figs. S6 and S7 of SI.

As suggested by the soft XAS results, the Cu valence state changes from divalent (Cu^{2+}) to monovalent cation (Cu^+) in the doping process. The ionic radii of Zn^{2+} , Cu^{2+} , and Cd^{2+} are 74 pm, 73 pm, and 95 pm, respectively. The Cu dopant into CdS results in a shift of the XRD peaks owing to the obvious difference of radii between Cu^{2+} and Cd^{2+} [50]. However, our XRD results indicate

that there is no obvious peak shift in comparison with the undoped and doped ZCS (Fig. 1(a)). The Cu substitution of Cd should result in lattice reduction, which is not observed. Hence, we only study the situation of substitution of Zn by Cu atoms (Cu_{Zn}).

Two important issues with quaternary semiconductors are as follows: (i) The equilibrium growth conditions of Cu-ZCS (e.g., chemical potentials of each constituent species), (ii) The formation of two CuZn^{1-} adjacent to a sulfur vacancy V_S^{2+} ($2\text{Cu}_{\text{Zn}}\text{V}_S^{2+}$) in ZCS crystal. To describe the phase stability of Cu-ZCS relative to the secondary compounds, the stability region in the atomic chemical potential landscape has been calculated, as shown in Fig. 5(a) and (b). At Cu-rich ($\Delta\mu_{\text{Cu}}=0$ eV) condition, the black area in Fig. 5(a) indicates the stable regions. As Cu becomes poorer ($\Delta\mu_{\text{Cu}}=-0.30$ eV), the black area changes with $\Delta\mu_{\text{Cu}}$ and becomes larger (Fig. 5(b)). As we can see, the volume of the stable region is not large, and a deviation outside this space will cause the formation of CuS, ZnS, CdS, or Cu_2S . The narrow thermodynamic window demonstrates that chemical-potential control is important for the growth of high-quality crystals. In particular, the stable region is narrow along the μ_{Zn} axis, thus the control of Zn content is crucial.

To answer whether Cu substitution of Zn by Cu atoms (2Cu_{Zn}) and the formation of two CuZn^{1-} adjacent to a sulfur vacancy V_S^{2+} ($2\text{Cu}_{\text{Zn}}\text{V}_S^{2+}$) in ZCS crystal are easy to be processed, we calculated the formation energies as a function of the Fermi energy as shown in Fig. 5(c) and (d). The thermodynamic chemical-potential point A of stable region (Fig. 5(a)) is chosen as the growth conditions. We see that as the Fermi energy shifts up from the valence to conduction band in Fig. 5(c), the formation of $\text{Cu}_{\text{Zn}}^{1-}$ is more favorable, which agrees well with experimental observations of Car et al. who found the $2\text{Cu}_{\text{Zn}}^{1-}\text{V}_S$ complex in ZnS nanocrystals using the extended X-ray absorption fine structure

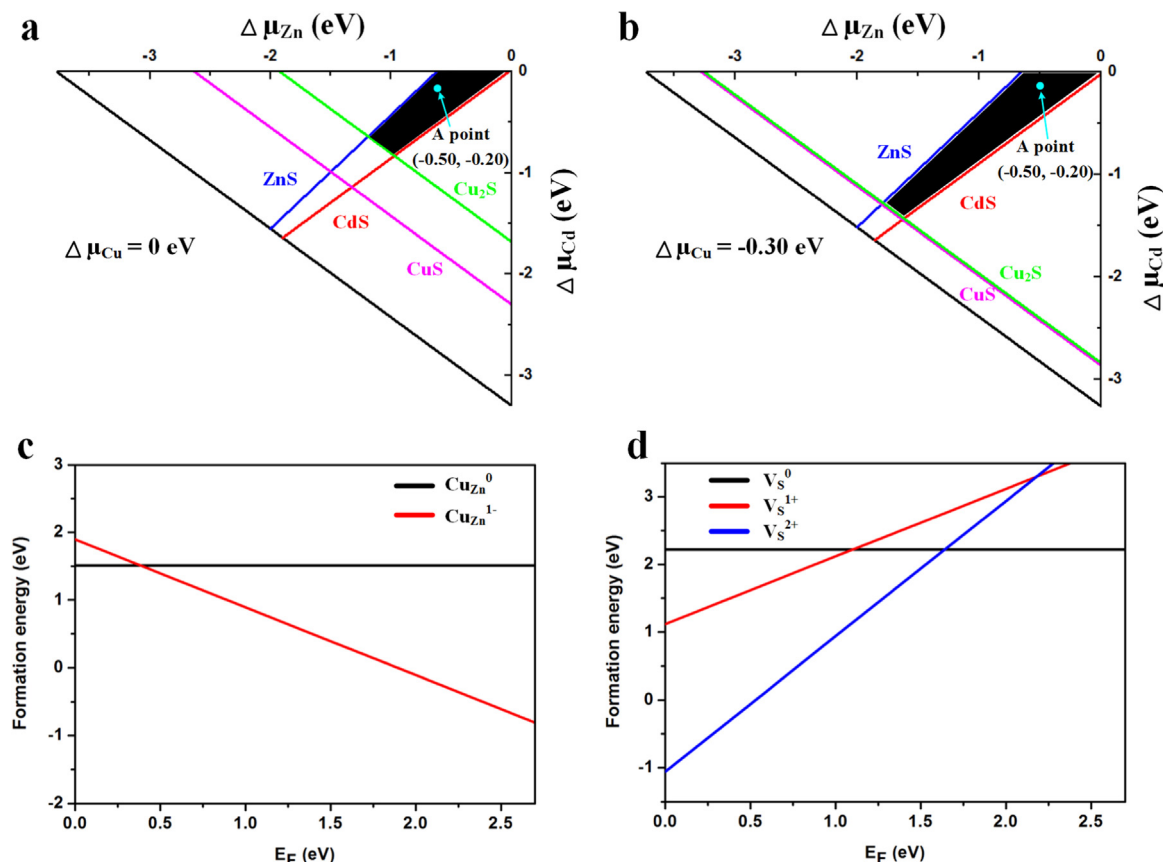


Fig. 5. The calculated chemical-potential stability diagram of Cu-ZCS in (a) Cu-rich ($\Delta\mu_{\text{Cu}}=0$ eV) and (b) Cu-poor plane ($\Delta\mu_{\text{Cu}}=-0.30$ eV); all values are in eV. And Formation energy of (c) Cu substitution (Cu_{Zn}) and (d) S vacancy (V_S) as a function of Fermi energy in cubic ZCS model.

(EXAFS) [49]. With the same methodology, Gul et al. also found the $2\text{Cu}_{\text{Zn}}^{1-}\text{V}_{\text{Se}}$ in ZnSe nanocrystals [47]. In contrast to the $\text{Cu}_{\text{Zn}}^{1-}$, the formation energy of V_{S}^{1+} and V_{S}^{2+} in ZCS crystal increases as the Fermi energy moves towards the conduction band due to the energy penalty associated with additional high-energy electron carriers.

Furthermore, we also calculated the V_{S}^0 formation energies in ZCS and Cu-ZCS model under S-poor conditions, respectively. We found that the V_{S} formation energies decrease from 1.55 eV to -2.02 eV from the undoped bulk-ZCS to the Cu^+ -doped bulk-ZCS, and from 1.19 eV to -2.14 eV from the undoped ZCS(110) to the Cu^+ -doped ZCS(110) surface, respectively. These results demonstrate that the Cu dopant assists the spontaneous formation of S vacancies, which is consistent with previous studies [36]. Meanwhile, we calculated the lattice change of Cu^+ -doped ZCS based on the above model. It is found that the Zn-S bond length is increased by 0.01 Å after the Cu dopant. This trend is proved by the hard X-ray characterization, which displays about 0.05–0.08 Å of expansion of Zn-S bond length in Cu-ZCS(1% and 3%) except the unusually small change for Cu-ZCS(2%) (Fig. S13). It is still under investigation for why there was negligible change of Zn-S bond length in Cu-ZCS(2%).

Next, we examined the influence of the Cu^+ and S vacancy on the performance of photocatalytic H_2 evolution via the photoluminescence (PL) emission spectra of ZCS and Cu-ZCS(1–5%). The PL spectra in Fig. 6(a) exhibit a sharp peak for the undoped ZCS, and broad peaks with red shift for the doped Cu-ZCS(1–5%). The sharp PL band for ZCS centered at 597 nm can be ascribed to the surface defects of ZCS [51]. The broad PL peaks for the doped Cu-ZCS(1–5%) originate from the trap-level emissions [52]. To illustrate this point, the density of states (DOS) and local density of states (LDOS) of with S vacancy and Cu^+ -dopant in the bulk of ZCS are shown in Fig. 6(b). There are three states in the band gap, including a bonding V_{S} , a bonding Cu, and an antibonding (V_{S}^*) state. The presence of these states caused by the Cu^+ -dopant enhances the absorbance of Cu-ZCS(1–5%) catalysts, as shown in Fig. 1(b). Meanwhile, these states in Cu-ZCS(1–5%) catalysts also can act as recombination centers of photogenerated e^-/h^+ pairs, causing the broad red emission peaks. The DOS of ZCS, ZCS with S vacancy, and Cu^+ -doped ZCS are shown in Fig. S14. Compared with the clean ZCS, the S vacancy or Cu^+ -dopant greatly reduces the band gap of ZCS.

We sought to clarify why the presence of Cu^+ -dopants significantly improves the photocatalytic activities. To this end, we analyzed the electronic structure of the ZCS(110) and ZCS(111) surfaces with and without S vacancy or Cu^+ -dopant, as shown in

Figs. S15 and S16. It is found that V_{S} induces two states in the band gap, bonding V_{S} and an antibonding (V_{S}^*) states like in the bulk phase, which can act as trapping sites for the photoexcited carriers [3]. After the Cu doping, the LDOS of Cu dopants show that the main Cu peaks locate at the energy range of 0.00–3.00 eV below the valence band maximum (VBM), however, a few states are slightly above the VBM. This suggests that Cu dopants caused some band edge states and likely act as acceptors of photoexcited holes. It has already been proved by the *in situ* electron paramagnetic resonance (EPR) characterization of Cu^+ -doped ZnS under 365 nm of UV-light irradiation, saying the Cu^+ would accept one hole and change into Cu^{2+} [53]. According to our calculations, this is true for both bulk Cu doping and surface Cu doping.

Fig. 7(a) and Fig. S17(a) are 3D isosurface contour plots of the VBM (highest occupied molecular orbital) and CBM (lowest unoccupied molecular orbital) for the (110) and (111) surfaces, respectively. On the ZCS(110) and ZCS(111) surfaces, we find that either the spatial distribution of holes or electrons is mainly located on the surface Zn atoms (being adjacent to S vacancies) and S atoms. However, the Cu^+ -dopant changes the distribution of the holes (VBM states) and electrons (CBM states), as shown in Fig. 7(b) and Fig. S17(b). It is clear that the holes of the (110) and (111) surfaces are located on the Cu^+ atoms; however, the electrons are located on the surface Zn atoms being adjacent to the S vacancy, respectively. The DOS and LDOS analyses shown in Figs. S15 and S16 are consistent with the charge density distribution results.

By combining the experimental measurements and theoretical calculations, we propose the following mechanism for the effects of Cu^+ -dopant to the photocatalytic HER: the doping of Cu in bulk or surface will introduce tail states. This will increase the light absorption of the visible lights, which is one of the driving forces for the increase of AQE. On the other hand, the Cu^+ -dopant will also induce the formation of S vacancy (V_{S}), and the Cu^+ and V_{S} both in bulk and surface will attract the photoexcited h^+ and e^- (Figs. 7 and S18), respectively. This will increase the separation ability of the photoexcited carriers. Since the electron and hole will be attracted near the $2\text{Cu}^+/\text{V}_{\text{S}}$ surface defect complex, there is a further possibility that the $2\text{Cu}^+/\text{V}_{\text{S}}$ can serve as a catalytic center, although further studies are needed to test this idea. As mentioned in the photocatalytic performance part, Cu-ZCS(2%) sample reaches the highest photocatalytic H_2 evolution rate among Cu-ZCS(1–5%) under the same condition. Although the Cu^+ dopant and S vacancy can attract the photoexcited carriers, they can also partly act as recombination center because they form discrete levels in $\text{Zn}_{0.5}\text{Cd}_{0.5}\text{S}$ semiconductor (Fig. 6(b)). The Cu-ZCS(2%)

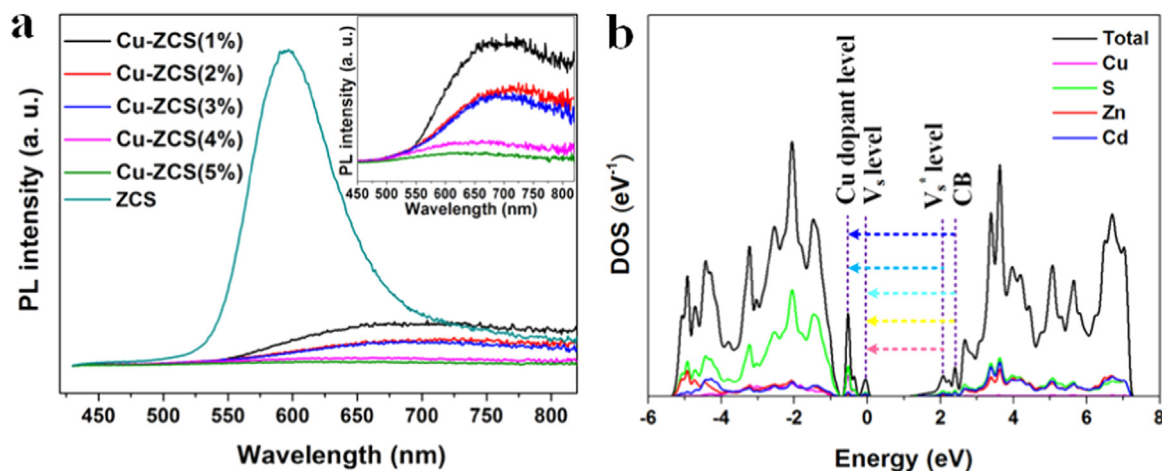


Fig. 6. (a) PL spectra of the ZCS, and Cu-ZCS(1–5%); and (b) DOS and LDOS of Cu-ZCS(1–5%), along with the CB, V_{S}^* level, V_{S} level, and Cu dopant level.

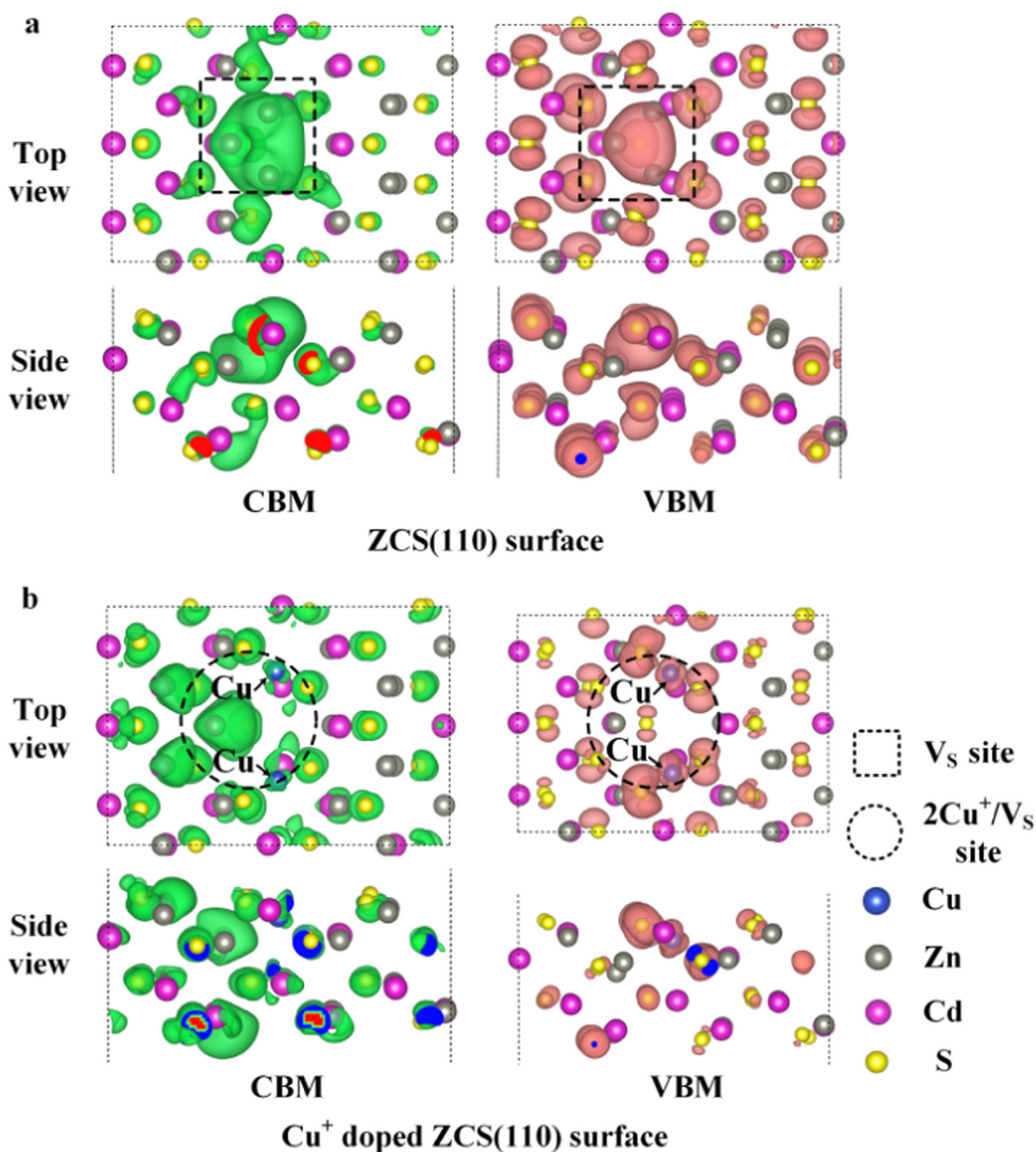


Fig. 7. Top and side view of the charge density of the electronic states in the energy range 0.00–0.50 eV below VBM and 0.00–0.50 eV above CBM: (a), ZCS(110) with S vacancy, (b) Cu^+ -doped ZCS(110).

sample must show the best balance between the roles of suppressing recombination and the recombination center, then it show the highest photocatalytic activity. The dose of Cu dopant is in agreement with the previous work for the highest efficient photocatalyst [15].

7. Conclusions

In summary, Cu^+ -doped $\text{Zn}_{0.5}\text{Cd}_{0.5}\text{S}$ nanocrystals have been successfully synthesized, and the mechanism resulting in the different photocatalytic H_2 evolution performance has also been carefully studied by experimental and theoretical methods. We found that the Cu^+ -dopant and S vacancies in mesoporous

$\text{Zn}_{0.5}\text{Cd}_{0.5}\text{S}$ was crucial to enhance the photocatalytic activities. The improved activities were attributed to the enhanced visible light absorption and improved separation ability of photoexcited carriers. Our findings can provide useful information for the development of more efficient photocatalysts or photovoltaic materials.

Acknowledgments

The authors acknowledge the financial support from National Project for EV Batteries (20121110, OptimumNano, Shenzhen), Guangdong Innovation Team Project (No. 2013N080), the use of

the Advanced Photon Source of Argonne National Laboratory supported by the U. S. Department of Energy, Office of Science, Office of Basic Energy Sciences. PNC/XSD facilities at the Advanced Photon Source, and research at these facilities, are supported by the US Department of Energy-Basic Energy Sciences, a Major Resources Support grant from NSERC, the University of Washington, the Canadian Light Source and the Advanced Photon Source (AC02-06CH11357).

Appendix A. Supplementary material

Supplementary data associated with this article can be found in the online version at <http://dx.doi.org/10.1016/j.nanoen.2016.05.051>.

References

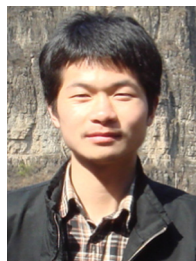
- [1] Y. Sang, Z. Zhao, M. Zhao, P. Hao, Y. Leng, H. Liu, *Adv. Mater.* 27 (2015) 363–369.
- [2] Q. Liang, Z. Li, X. Yu, Z.-H. Huang, F. Kang, Q.-H. Yang, *Adv. Mater.* 27 (2015) 4634–4639.
- [3] X. Chen, L. Liu, P.Y. Yu, S.S. Mao, *Science* 331 (2011) 746–750.
- [4] H. Song, L. Zhu, Y. Li, Z. Lou, M. Xiao, Z. Ye, *J. Mater. Chem. A* 3 (2015) 8353–8360.
- [5] H. Zheng, J.Z. Ou, M.S. Strano, R.B. Kaner, A. Mitchell, K. Kalantar-zadeh, *Adv. Funct. Mater.* 21 (2011) 2175–2196.
- [6] G. Rothenberger, J. Moser, M. Grätzel, N. Serpone, D.K. Sharma, *J. Am. Chem. Soc.* 107 (1985) 8054–8059.
- [7] H. Tong, S. Ouyang, Y. Bi, N. Umezawa, M. Oshikiri, J. Ye, *Adv. Mater.* 24 (2012) 229–251.
- [8] Q. Han, B. Wang, Y. Zhao, C. Hu, L. Qu, *Angew. Chem. Int. Ed.* 54 (2015) 11433–11437.
- [9] X. She, L. Liu, H. Ji, Z. Mo, Y. Li, L. Huang, D. Du, H. Xu, H. Li, *Appl. Catal. B: Environ.* 187 (2016) 144–153.
- [10] N. Zhang, S. Ouyang, T. Kako, J. Ye, *Chem. Commun.* 48 (2012) 1269–1271.
- [11] Z. Mei, S. Ouyang, Y. Zhang, T. Kako, *RSC Adv.* 3 (2013) 10654–10657.
- [12] I. Tsuji, H. Kato, H. Kobayashi, A. Kudo, *J. Am. Chem. Soc.* 126 (2004) 13406–13413.
- [13] I. Tsuji, H. Kato, A. Kudo, *Angew. Chem. Int. Ed.* 44 (2005) 3565–3568.
- [14] I. Tsuji, H. Kato, A. Kudo, *Chem. Mater.* 18 (2006) 1969–1975.
- [15] Y. Li, G. Chen, Q. Wang, X. Wang, A. Zhou, Z. Shen, *Adv. Funct. Mater.* 20 (2010) 3390–3398.
- [16] Y. Li, G. Chen, C. Zhou, J. Sun, *Chem. Commun.* 15 (2009) 2020–2022.
- [17] M. Liu, L. Wang, G. Lu, X. Yao, L. Guo, *Energy Environ. Sci.* 4 (2011) 1372–1378.
- [18] Y. Wang, J. Wu, J. Zheng, R. Xu, *Catal. Sci. Technol.* 1 (2011) 940–947.
- [19] Q. Li, H. Meng, P. Zhou, Y. Zheng, J. Wang, J. Yu, *J. Gong. ACS Catal.* 3 (2013) 882–889.
- [20] J. Zhang, J. Yu, M. Jaroniec, J. Gong, *Nano Lett.* 12 (2012) 4584–4589.
- [21] L. Wang, Z. Yao, F. Jia, B. Chen, Z. Jiang, *Dalton Trans.* 42 (2013) 9976–9981.
- [22] J. Zhang, L. Qi, J. Ran, J. Yu, S.-Z. Qiao, *Adv. Energy Mater.* 4 (2014) 1301925.
- [23] Y. Wang, J. Wu, J. Zheng, R. Jiang, R. Xu, *Catal. Sci. Technol.* 2 (2012) 581–588.
- [24] X. Zhang, D. Jing, L. Guo, *Int. J. Hydrog. Energy* 35 (2010) 7051–7057.
- [25] K. Zhang, Z. Zhou, L. Guo, *Int. J. Hydrog. Energy* 36 (2011) 9469–9478.
- [26] K. Zhang, D. Jing, Q. Chen, L. Guo, *Int. J. Hydrog. Energy* 35 (2010) 2048–2057.
- [27] Y.-G. Yu, G. Chen, L.-X. Hao, Y.-S. Zhou, Y. Wang, J. Pei, J.-X. Sun, Z.-H. Han, *Chem. Commun.* 49 (2013) 10142–10144.
- [28] W. Zhang, Z. Zhong, Y. Wang, R. Xu, *J. Phys. Chem. C* 112 (2008) 17635–17642.
- [29] J. Zhang, Q. Xu, S.-Z. Qiao, J. Yu, *ChemSusChem* 6 (2013) 2009–2015.
- [30] W. Zhang, R. Xu, *Int. J. Hydrog. Energy* 34 (2009) 8495–8503.
- [31] S. Xiao, P. Liu, W. Zhu, G. Li, D. Zhang, H. Li, *Nano Lett.* 15 (2015) 4853–4858.
- [32] P. Hohenberg, W. Kohn, *Phys. Rev.* 136 (1964) B864–B871.
- [33] W. Kohn, L.J. Sham, *Phys. Rev.* 140 (1965) A1133–A1138.
- [34] J.P. Perdew, K. Burke, M. Ernzerhof, *Phys. Rev. Lett.* 77 (1996) 3865–3868.
- [35] G. Kresse, D. Joubert, *Phys. Rev. B* 59 (1999) 1758–1775.
- [36] H.H. Pham, G.T. Barkema, L.W. Wang, *Phys. Chem. Chem. Phys.* 17 (2015) 26270–26276.
- [37] H. Raebiger, S. Lany, A. Zunger, *Nature* 453 (2008) 763–766.
- [38] D. Zherebetskyy, M. Scheele, Y. Zhang, N. Bronstein, C. Thompson, D. Britt, M. Salmeron, P. Alivisatos, L.W. Wang, *Science* 344 (2014) 1380–1384.
- [39] W. Yang, X. Liu, R. Qiao, P. Olalde-Velasco, J.D. Spear, L. Rosegio, J.X. Pepper, Y. D. Chuang, J.D. Denlinger, Z. Hussain, *J. Electron Spectrosc. Relat. Phenom.* 190 (2013) 64–74.
- [40] Q. He, X. Yang, R. He, A. Bueno-López, H. Miller, X. Ren, W. Yang, B.E. Koel, *J. Power Sources* 213 (2012) 169–179.
- [41] C.L. Chen, K.W. Yeh, D.J. Huang, F.C. Hsu, Y.C. Lee, S.W. Huang, G.Y. Guo, H.-J. Lin, S.M. Rao, M.K. Wu, *Phys. Rev. B* 78 (2008) 214105.
- [42] J. Xu, X. Yang, Q.-D. Yang, T.-L. Wong, C.-S. Lee, *J. Phys. Chem. C* 116 (2012) 19718–19723.
- [43] H. Azimi, S. Kuhri, A. Osvet, G. Matt, L.S. Khazada, M. Lemmer, N. A. Luechinger, M.I. Larsson, E. Zeira, D.M. Guldi, C.J. Brabec, *J. Am. Chem. Soc.* 136 (2014) 7233–7236.
- [44] Y. Zhang, T. Qiao, X. Hu, *J. Cryst. Growth* 268 (2004) 64–70.
- [45] Q. Wang, G. Yun, Y. Bai, N. An, Y. Chen, R. Wang, Z. Lei, W. Shangguan, *Int. J. Hydrog. Energy* 39 (2014) 13421–13428.
- [46] J.R. Vegelius, K.O. Kvashnina, H. Hollmark, M. Klintonberg, Y.O. Kvashnin, I. L. Soroka, L. Werme, S.M. Butorin, *J. Phys. Chem. C* 116 (2012) 22293–22300.
- [47] S. Gul, J.K. Cooper, P.-A. Glans, J. Guo, V.K. Yachandra, J. Yano, J.Z. Zhang, *ACS Nano* 7 (2013) 8680–8692.
- [48] J.K. Cooper, S. Gul, S.A. Lindley, J. Yano, J.Z. Zhang, *ACS Appl. Mater. Interfaces* 7 (2015) 10055–10066.
- [49] B. Car, S. Medling, C. Corrado, F. Bridges, J.Z. Zhang, *Nanoscale* 3 (2011) 4182–4189.
- [50] P. Reyes, S. Velumani, *Mater. Sci. Eng. B* 177 (2012) 1452–1459.
- [51] J. Shi, H. Cui, Z. Liang, X. Lu, Y. Tong, C. Su, H. Liu, *Energy Environ. Sci.* 4 (2011) 466–470.
- [52] Z.-X. Yang, P. Zhang, W. Zhong, Y. Deng, C.-T. Au, Y.-W. Du, *CrystEngComm* 14 (2012) 4298–4305.
- [53] W.C. Holton, M.D. Wit, R.K. Watts, T.L. Estle, J. Schneider, *J. Phys. Chem. Solids* 30 (1969) 963–977.



Zongwei Mei is currently a Lecture at School of Advanced Materials (SAM), Peking University, Shenzhen Graduate School, China. He received his Ph.D. in Chemistry in 2013 from Hokkaido University, Japan. Then he worked as a post-doctoral fellow from Apr. 2014 to Apr. 2016 in Prof. Feng Pan's group at SAM. His research interests focus on the development, properties, and mechanism of photocatalytic/photoelectrochemical materials, and the catalyst for oxygen reduction (ORR) and oxygen evolution reaction (OER) in metal-air battery.



Bingkai Zhang received the Ph.D. degree from Huazhong University of Science and Technology, China, in 2014. Then, He is currently a postdoctoral researcher in Peking University, China. His main research fields are computational materials design and materials for energy storage and conversion.



Jiaxin Zheng received his BSc in Physics in 2008 and Ph.D. degree in Condensed Matter Physics in 2013 from Peking University, China. Then he joined the group of Prof. Feng Pan at School of Advanced Materials (SAM), Peking University, Shenzhen Graduate School, China, as a post-doctoral fellow from Oct. 2013 to Oct. 2015. Now he works as an assistant Professor at SAM. His research interests include: computational materials, energy materials (battery materials, solar energy, thermoelectric materials), nanomaterials, nanoelectronics.



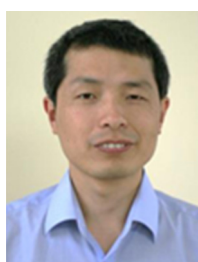
Sheng Yuan received his Bachelor's degree (BE) in 2014 from Guizhou University, China. He is currently a master student major in materials chemistry in Peking University Shenzhen graduate school. His research is mainly focused on photocatalytic materials and solar cells.



Zengqing Zhuo received his B. S. degree in 2013 from Energy and Resources Engineering, Peking University, China. He is pursuing his Ph.D. degree in the School of Advanced Materials, Peking University, China. His research interests include soft x-ray spectroscopy for lithium ion battery electrode materials and electrolyte system.



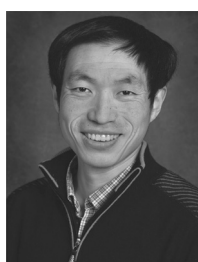
Xianguang Meng is currently a postdoctoral researcher in the group of Prof. Jinhua Ye in the Environment and Energy Materials Division, National Institute of Materials Science, Japan. He received his bachelor and master's degree from School of Materials Science and Engineering, Tianjin University, and his Ph.D. degree from Graduate School of Chemical Sciences and Engineering, Hokkaido University in 2015. His current research interests include the applications of semiconductor and nanometal materials for the activation and catalytic conversion of CO₂, H₂O, and CH₄ into renewable energy through the photo-, thermo- or electro-catalytic methods.



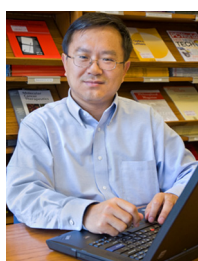
Zonghai Chen is currently a staff scientist of Argonne National Laboratory. He received his B. S. degree (1997) from University of Science and Technology of China, and Ph.D. degree (2004) from Dalhousie University. His research interest includes functional electrolytes and electrode materials for advanced lithium batteries, with particular focus on behavior of materials at extreme conditions.



Dr. Khalil Amine is a Distinguished Fellow and the Manager of the Advanced Battery Technology programs at Argonne National Laboratory, where he is responsible for directing the research and development of advanced materials and battery systems for HEV, PHEV, EV, satellite, military and medical applications. Dr. Amine currently serves a member of the U. S. National Research Consul on battery related technologies.



Wanli Yang received his B. S. in Physics from Shandong University, China (1995), and his Ph. D. in Condensed Matter Physics from Institute of Physics, Chinese Academy of Sciences (2000). He was a postdoctoral fellow at Stanford University, and then a staff scientist at the Geballe Laboratory for Adv. Mater. at Stanford University, working on photo-electron spectroscopy of nano materials. He has been a physicist scientist at the Advanced Light Source division of Lawrence Berkeley National Laboratory since 2006. His current research interests include novel instrumentation and methodology of employing soft X-ray spectroscopy for studying energy harvesting and storage materials.



Lin-Wang Wang: Senior Staff Scientist, Lawrence Berkeley National Laboratory, Berkeley, U. S. Dr. Wang has 25 years of experience in large scale electronic structure calculations. Worked with Alex Zunger, he invented the folded spectrum method. He developed a linear combination of bulk bands (LCBB) method for semiconductor heterostructure electronic structure calculations, generalized moments method, a popular parallel total energy plane wave pseudopotential program (PETot), and a linear scaling three dimensional fragment method (LS3DF). He invented a charge patching method, which enables the ab initio accuracy

thousand atom calculations for nanosystems. Recently, he developed a new algorithm for real-time time-dependent DFT calculations which accelerates the traditional algorithms by hundreds of times.



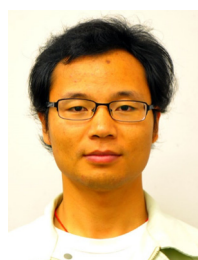
Wei Wang received his B. E. degree from Sichuan University in 2012. He is currently a Ph.D. student in the Institute of Modern Optics, School of Physics at Peking University under the supervision of Prof. Shufeng Wang. His current research interests focus on the dynamics in perovskite solar cells.



Shufeng Wang obtained his Ph.D. in 2001 in Physics Department, Peking University, China, with the guidance from Prof. Qihuang Gong. He worked as a postdoc with Prof. Dana D. Dlott at University of Illinois at Urbana-Champaign between 2001 and 2004. Now he is Associate Professor in School of Physics, Peking University, China. His research interests focus on nonlinear optics and ultrafast dynamics of photo-electronic materials and devices.



Qihuang Gong is now an Academician of the Chinese Academy of Sciences and a Professor in Department of Physics of Peking University, China. He received his BSc and Ph.D. (Joint training between China and English) from the Department of Physics of Peking University. He has published more than 300 papers with more than 2400 citations. His research interests focus on the femtosecond science and mesoscopic optics.



Jun Li has a Ph.D. in Chemistry from the Hokkaido University, two post-doctoral stints (at the National Institute for Materials Science and at University of Leuven). He is currently an associate professor at Nanjing University since 2014. His main research activities include micro- and nano-structured electronic devices, experimental high-temperature superconductors and superconducting devices, and low-dimensional energy devices.



Fu-Sheng Liu received his Ph.D. in condensed matter physics in 2005 from Institute of Physics, Chinese Academy of Sciences (CAS), China. From 2005 to now, he joined in Shenzhen University as a full professor. His current research interests include crystal structure, metallic functional materials, thermoelectric materials and their related properties. He has authored and co-authored more than 100 refereed journal publications.



Prof. Feng Pan, founding Dean of School of Advanced Materials, Peking University Shenzhen Graduate School, got B. S. from Dept. Chemistry, Peking University in 1985 and Ph.D. from Dept. of P&A Chemistry, University of Strathclyde, Glasgow, UK, with “Patrick D. Ritchie Prize” for the best p.H. D. in 1994. With more than a decade experience in large international incorporations, Prof. Pan has been engaged in fundamental research and product development of novel optoelectronic and energy storage materials and devices. As Chief Scientist, Prof. Pan led eight entities in Shenzhen to win the 150 million RMB grant for the national new energy vehicles (power battery) innovation project since 2013.